submitted to *Geophys. J. Int.*

Supplemental Material to:

The 2015–2017 Pamir Earthquake Sequence:

Fore-, Main-, and Aftershocks, Seismotectonics,

Fault Interaction, and Fluid Processes

Wasja Bloch[1,2⋆], Sabrina Metzger[1], Bernd Schurr[1], Xiaohui Yuan[1],

Lothar Ratschbacher[3], Sanaa Reuter[3], Qiang Xu[4,5], Junmeng Zhao[4,5],

Shokhruhk Murodkulov[6], Ilhomjon Oimuhammadzoda[7]

[1] *GFZ German Research Centre for Geosciences, 14473 Potsdam, Germany*

[2] *Department of Earth, Ocean and Atmospheric Sciences, University of British Columbia, Vancouver V6T 1Z4, Canada*

[3] *Geologie, Technische Universität Bergakademie Freiberg, 09599 Freiberg, Germany*

[4] *Key Laboratory of Continental Collision and Plateau Uplift, Institute of Tibetan Plateau Research,*

Chinese Academy of Sciences, Beijing 100101, China

[5] *CAS Center for Excellence in Tibetan Plateau Earth Sciences, Beijing 100101, China*

[6] *Institute of Geology, Earthquake Engineering and Seismology, National Academy of Sciences, Dushanbe, Tajikistan*

[7] *Department of Geology under the Government of the Republic of Tajikistan, Dushanbe, Tajikistan*

Contents of this file

(i) Video S1: Animated Map View of the Earthquake Sequence

(ii) Figs. S1 to S16

Additional Supporting Information (Files uploaded separately)

Video S1: Animated Map View on the Earthquake Sequence The video is an animated representation of Fig. 2a and b of the main text. Every audible ”click” represents one seismic event, the gain scales linear with earthquake magnitude. The events fade out within 100 days.

REFERENCES

Sippl, C., Schurr, B., Yuan, X., Mechie, J., Schneider, F., Gadoev, M., Orunbaev, S., Oimahmadov, I., Haberland, C., Abdybachaev, U., et al., 2013. Geometry of the Pamir-Hindu Kush intermediate-depth earthquake zone from local seismic data, *Journal of Geophysical Research: Solid Earth*, **118**(4), 1438–1457.

Utsu, T., Ogata, Y., et al., 1995. The centenary of the Omori formula for a decay law of aftershock activity, *Journal of Physics of the Earth*, **43**(1), 1–33.

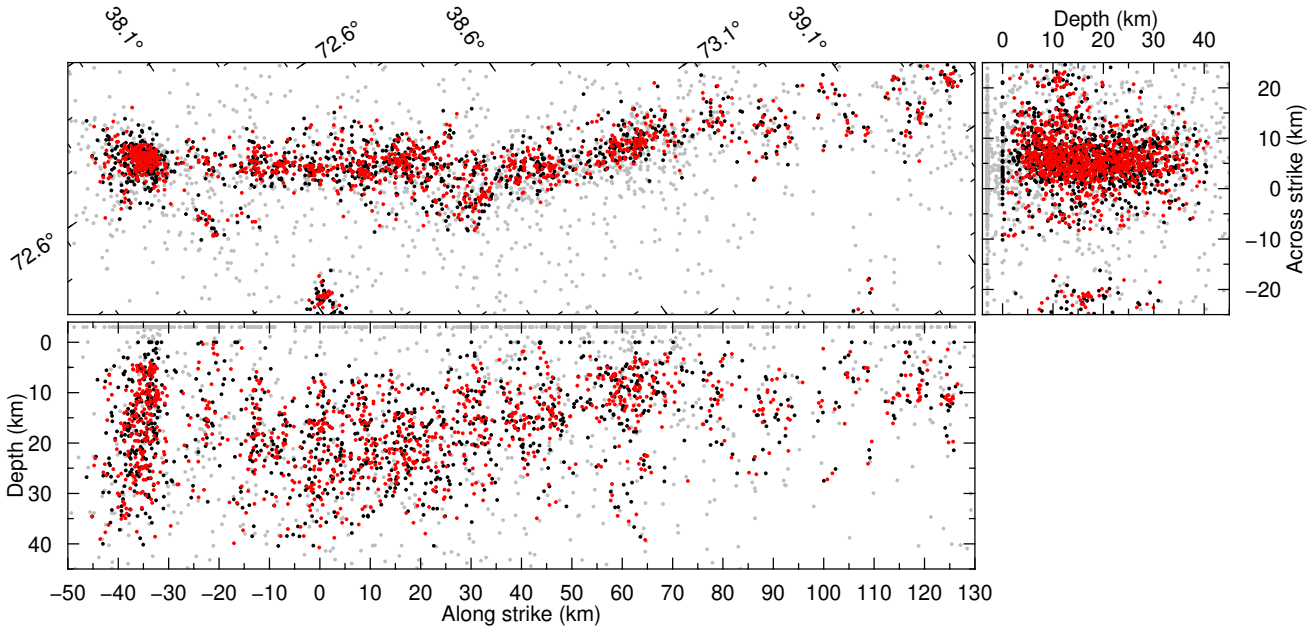

Figure S1. Comparison of event locations for the Sarez earthquake (Fig. 4 of the main text) after the different steps of the event location. Center panel: Map view. Right panel: across-strike profile. Lower panel: along-strike profile. Gray dots are hypocenters which could only be located with *simulps*, but not re-located. Black dots are hypocenters before and red dots after the re-location with *hypoDD*.

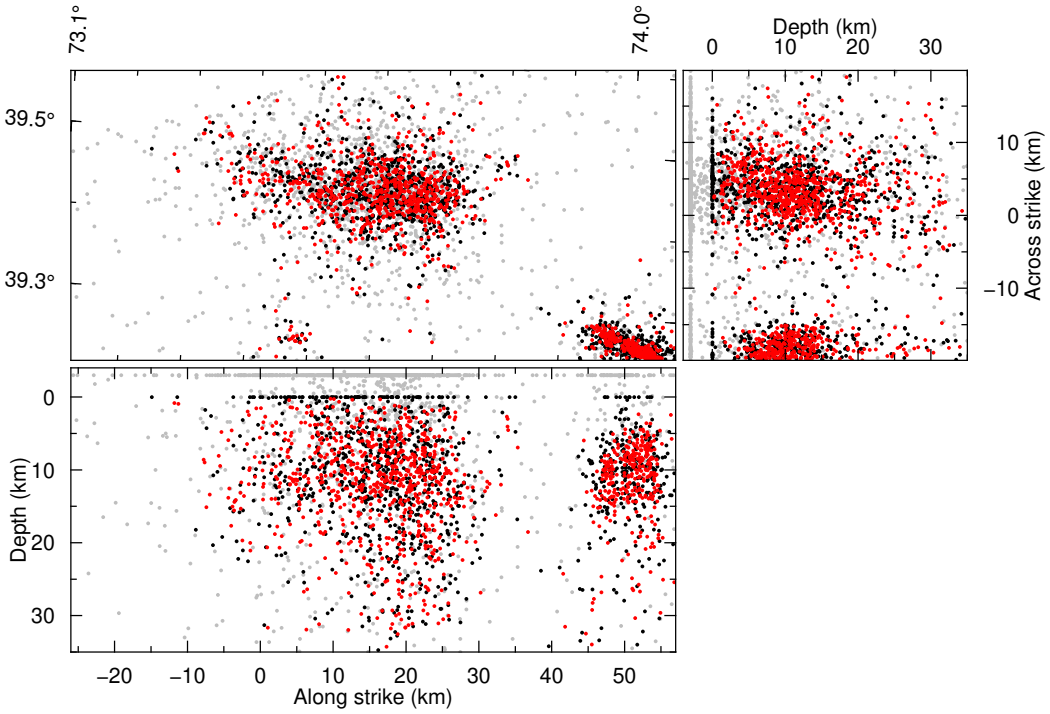

Figure S2. As Fig. S1, but for the Sary-Tash earthquake (Fig. 6 of the main text).

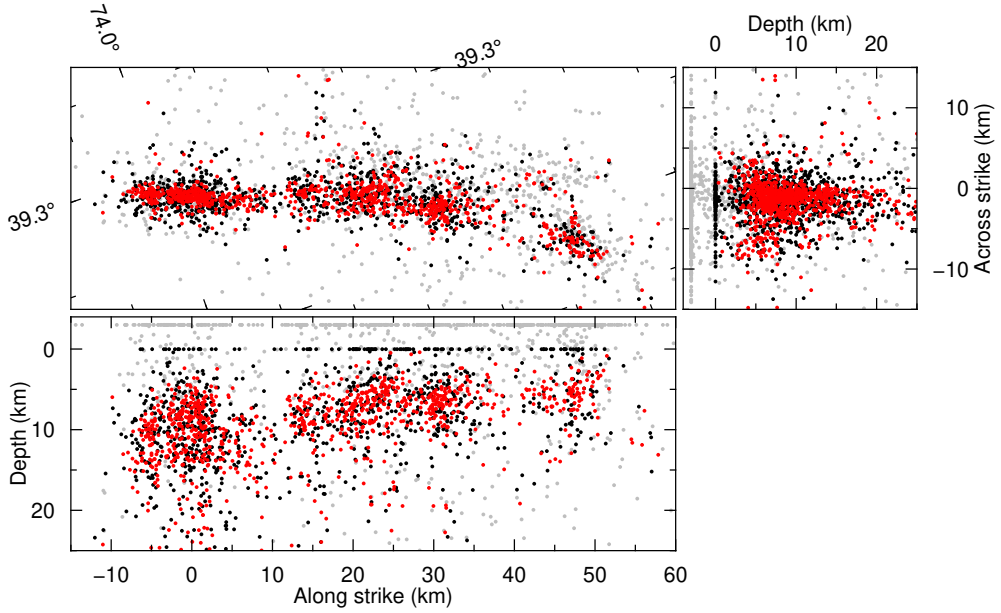

Figure S3. As Fig. S1, but for the Muji earthquake (Fig. 7 of the main text).

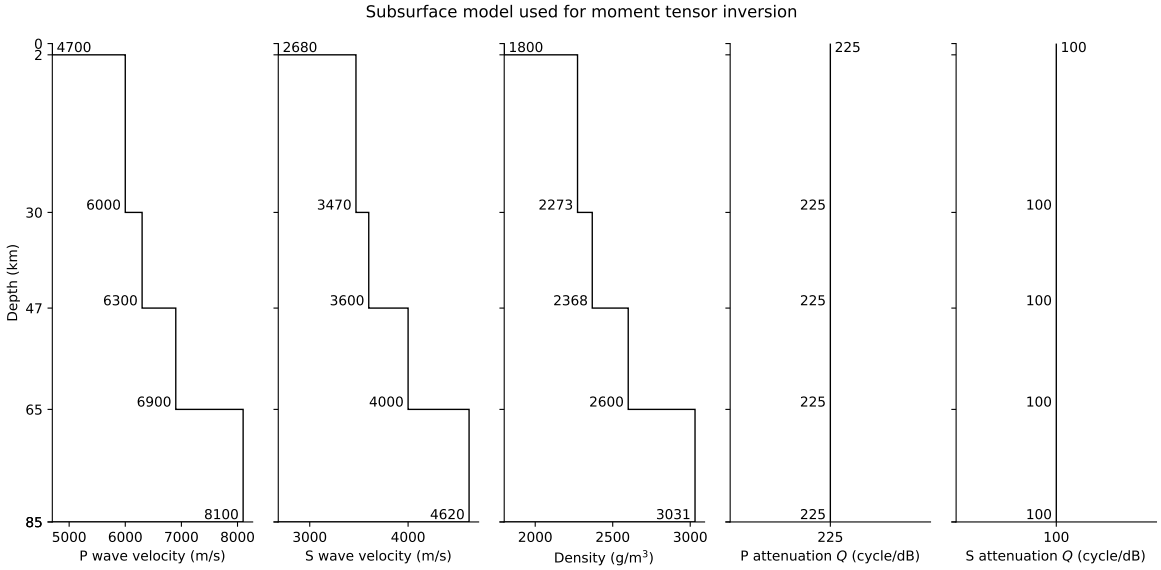

Figure S4. Subsurface model (Sippl et al. 2013) used for the determination of regional moment tensors.

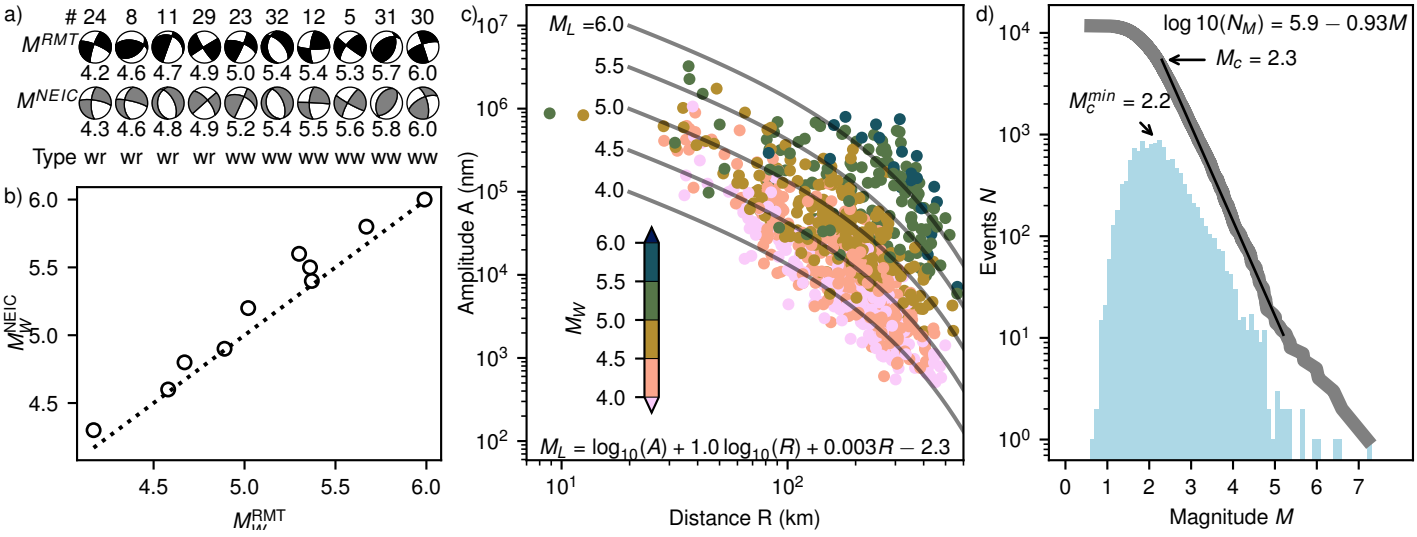

Figure S5. Moment magnitudes of seismic events. Comparison of regional moment tensors (a) and magnitudes (b) with results by NEIC. (wr) regional (ww) W-phase. (c) Calibration of local magnitudes with parameters of Equation 1 of the main text. (d) Magnitude distribution of the entire catalog. Completeness magnitude M_c, and most frequent magnitude M_c^{min}.

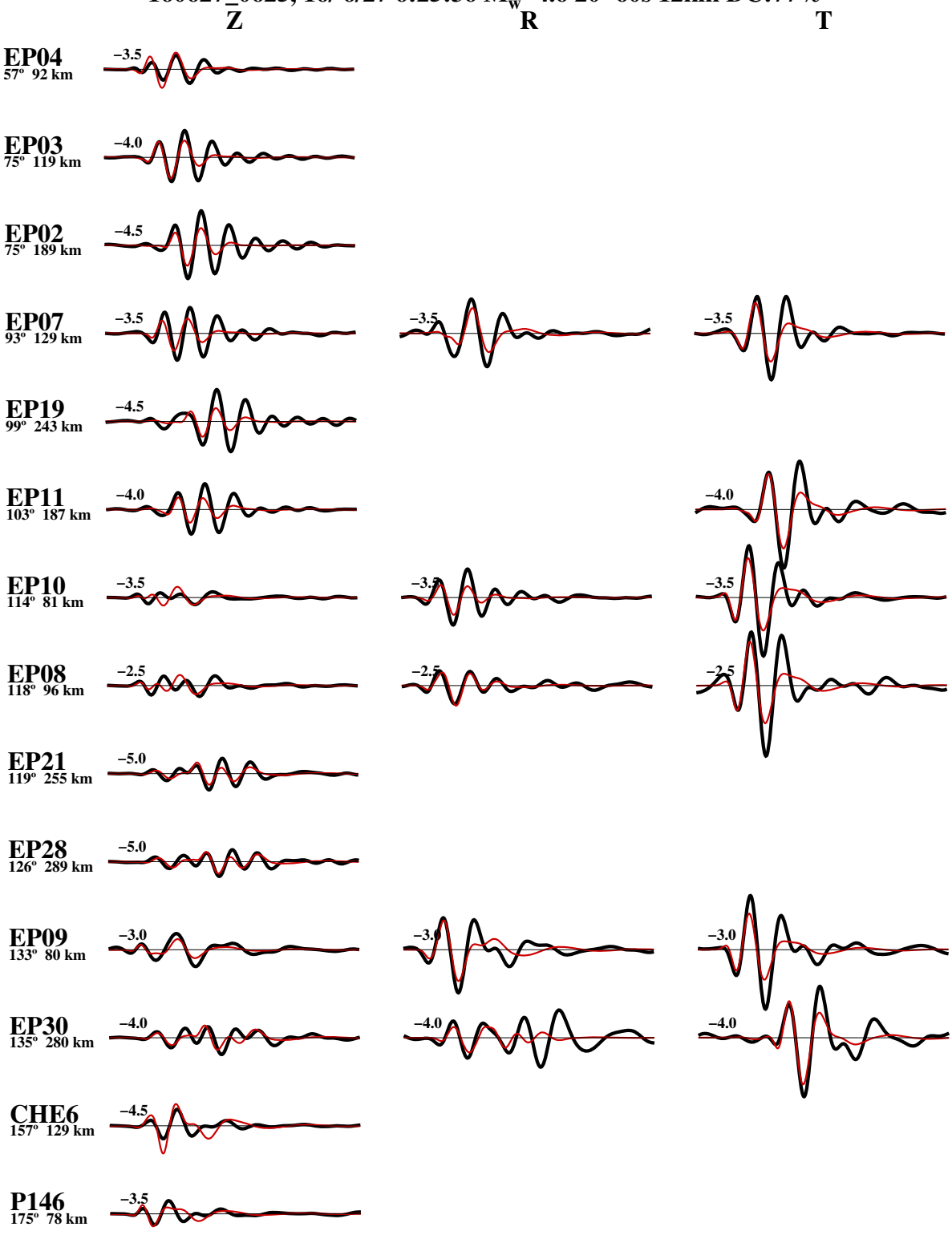
160627_0625, 16/ 6/27 6:25:36 M$_w$=4.6 20–60s 12km DC:77%
Z
R
T
EP04
57° 92 km
EP03
75° 119 km
EP02
75° 189 km
EP07
93° 129 km
EP19
99° 243 km
EP11
103° 187 km
EP10
114° 81 km
EP08
118° 96 km
EP21
119° 255 km
EP28
126° 289 km
EP09
133° 80 km
EP30
135° 280 km
CHE6
157° 129 km
P146
175° 78 km
−3.5
−4.0
−4.5
−3.5
−3.5
−3.5
−4.5
−4.0
−4.0
−3.5
−3.5
−3.5
−2.5
−2.5
−2.5
−5.0
−5.0
−3.0
−3.0
−3.0
−4.0
−4.0
−4.0
−4.5
−3.5

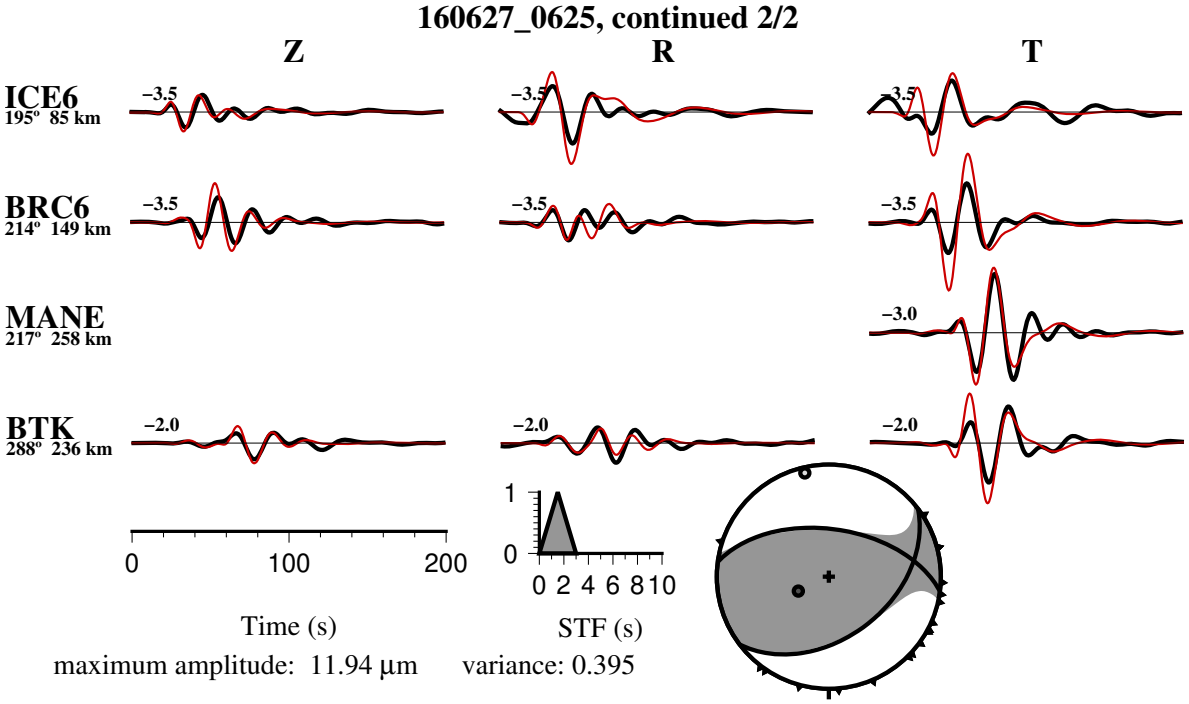

Figure S6. Results of moment tensor inversion for event 8 (Fig. S5), with observed (black) and modeled (red) waveforms for vertical (Z), radial (R) and transverse (T) component on the stations named on the left. Event back-azimuth and distance given below station name.

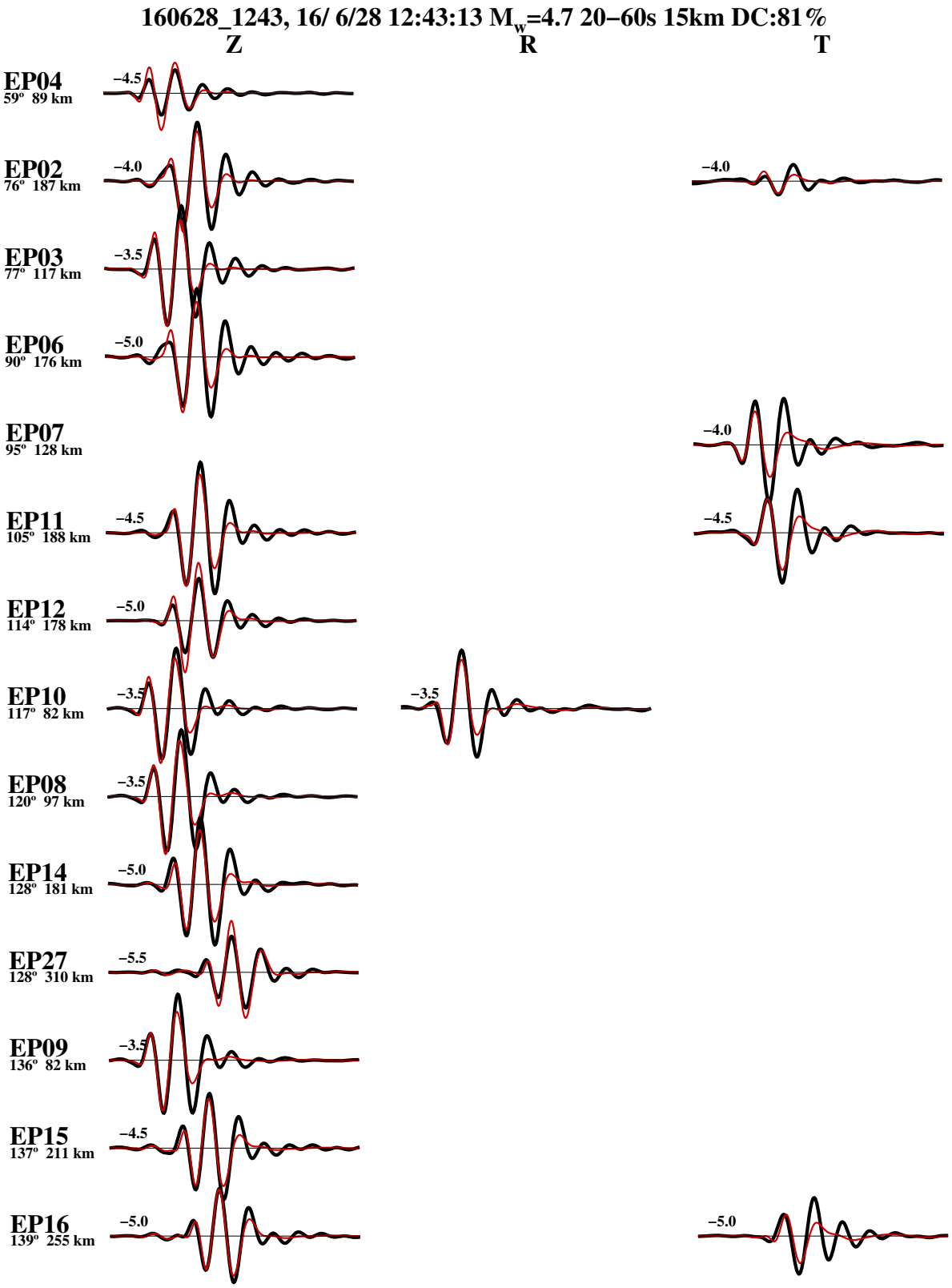
160628_1243, 16/ 6/28 12:43:13 M$_w$=4.7 20−60s 15km DC:81%
Z
R
T
EP04
59° 89 km
−4.5
EP02
76° 187 km
−4.0
−4.0
EP03
77° 117 km
−3.5
EP06
90° 176 km
−5.0
EP07
95° 128 km
−4.0
EP11
105° 188 km
−4.5
−4.5
EP12
114° 178 km
−5.0
EP10
117° 82 km
−3.5
−3.5
EP08
120° 97 km
−3.5
EP14
128° 181 km
−5.0
EP27
128° 310 km
−5.5
EP09
136° 82 km
−3.5
EP15
137° 211 km
−4.5
EP16
139° 255 km
−5.0
−5.0

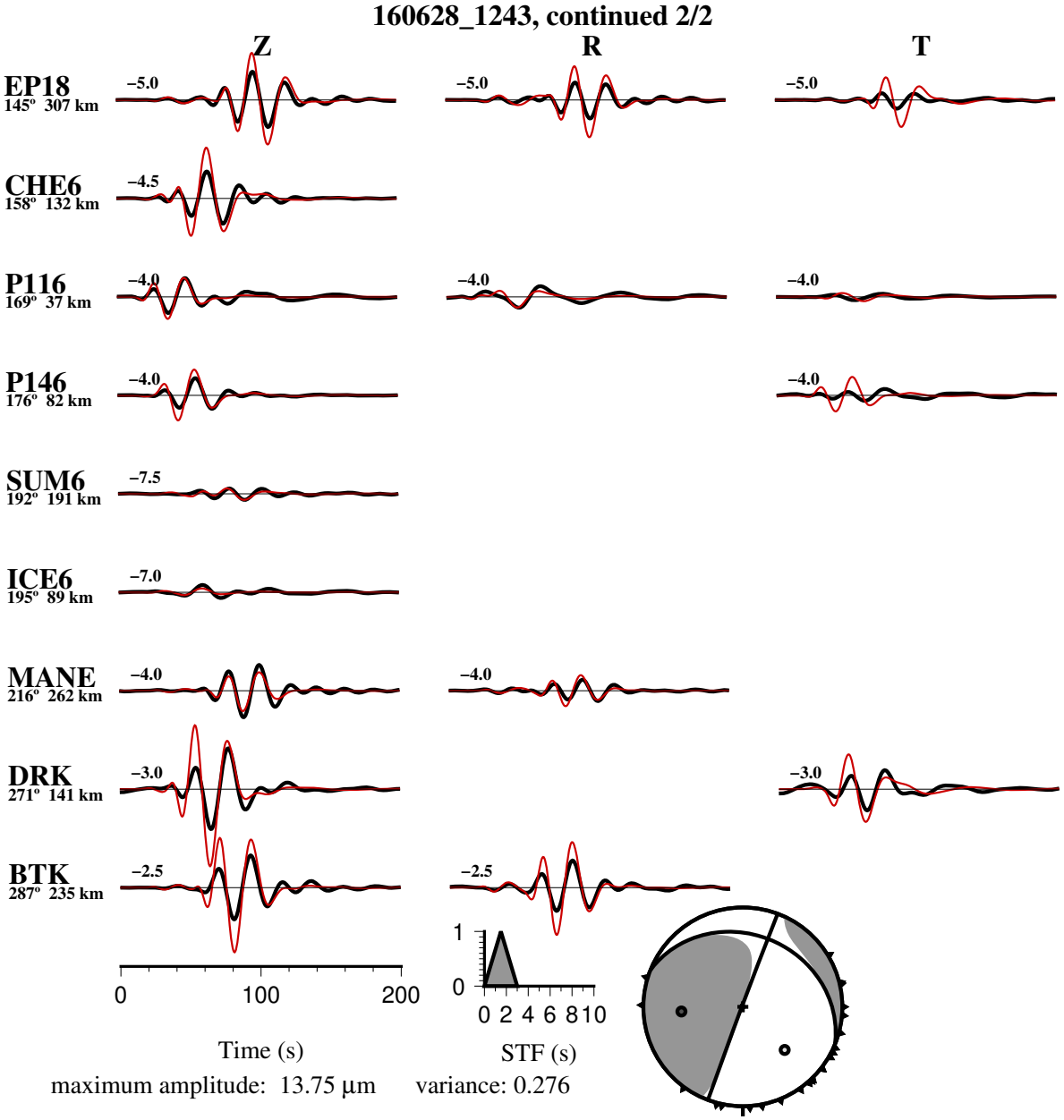

Figure S7. As Fig. S6, but for event 11 (Fig. S5).

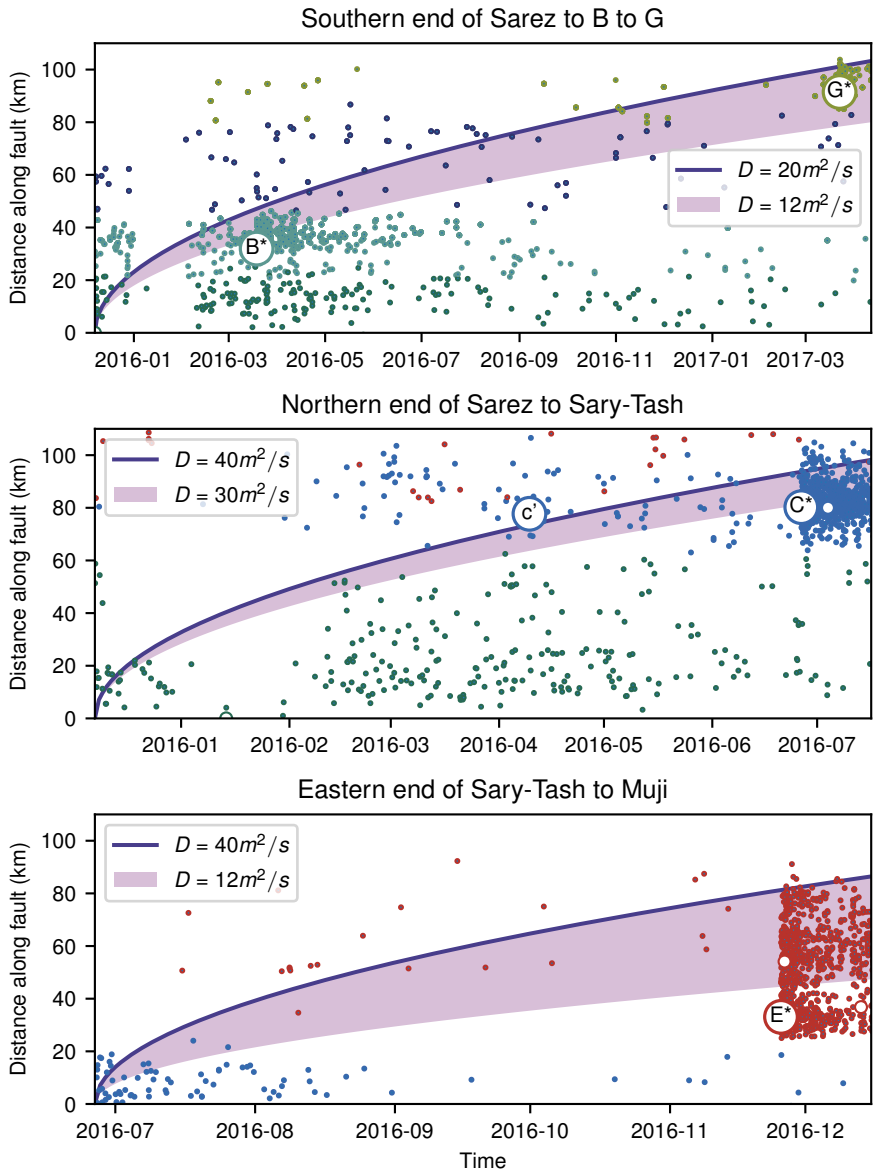

Figure S8. Spatio-temporal evolution of seismicity along the (top) southern continuation of the SKFS; (middle) northern continuation of the SKFS; (bottom) continuation of the MPTS into the Muji fault. D according to Equation 8 of the main text.

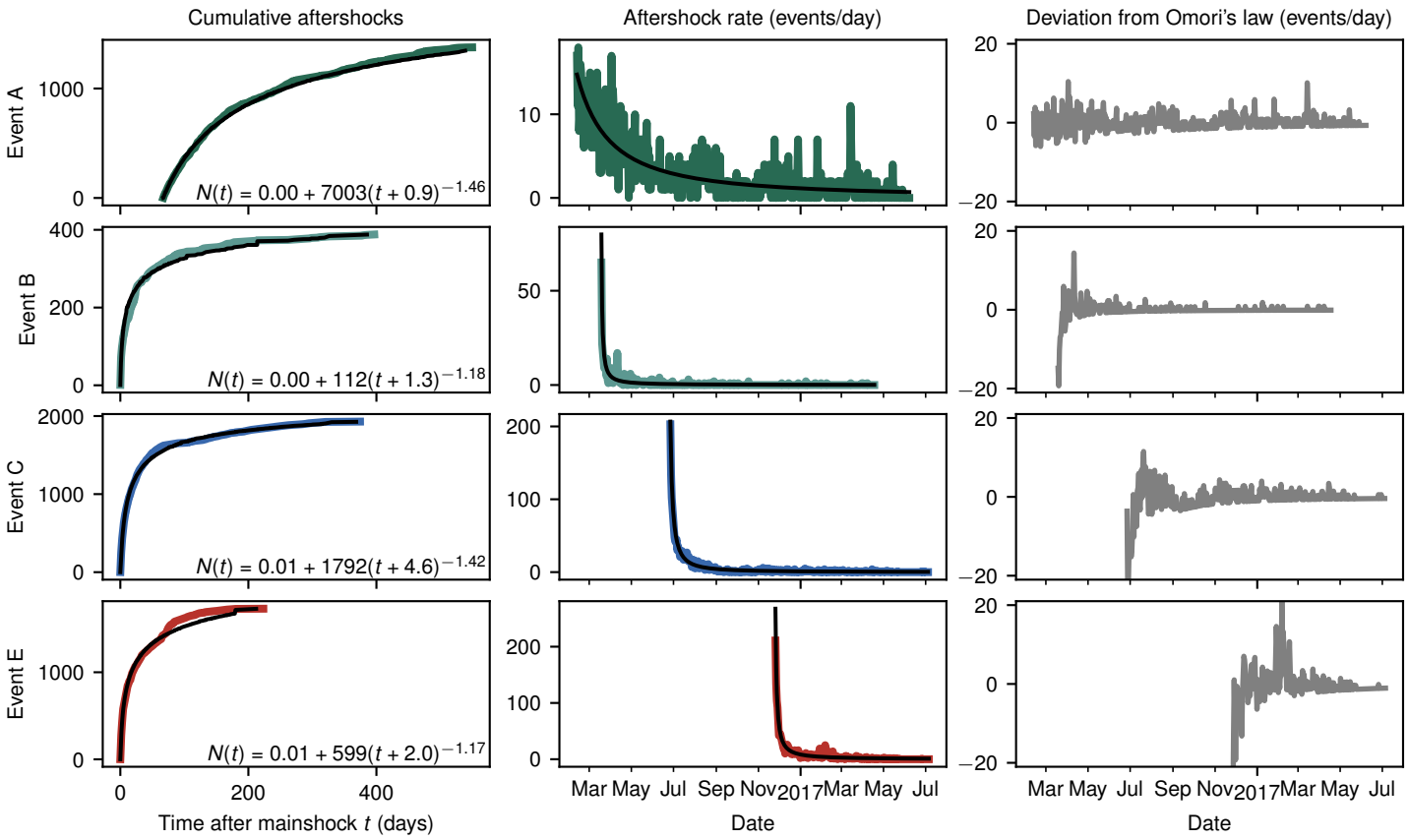

Figure S9. Aftershock characteristics of mainshock vicinities *A*, *B*, *C*, and *E*. Left column: Cumulative aftershocks after the mainshock (*A** only shown after installation of 8H network) and parameters of modified Omori's Law (Utsu et al. 1995). Middle column: Aftershock rate over time. Right column: Deviation of aftershock rate from Omori's law over time. Even though time intervals of increased aftershock activity exist, they to not correlate with each other in between earthquake sequences.

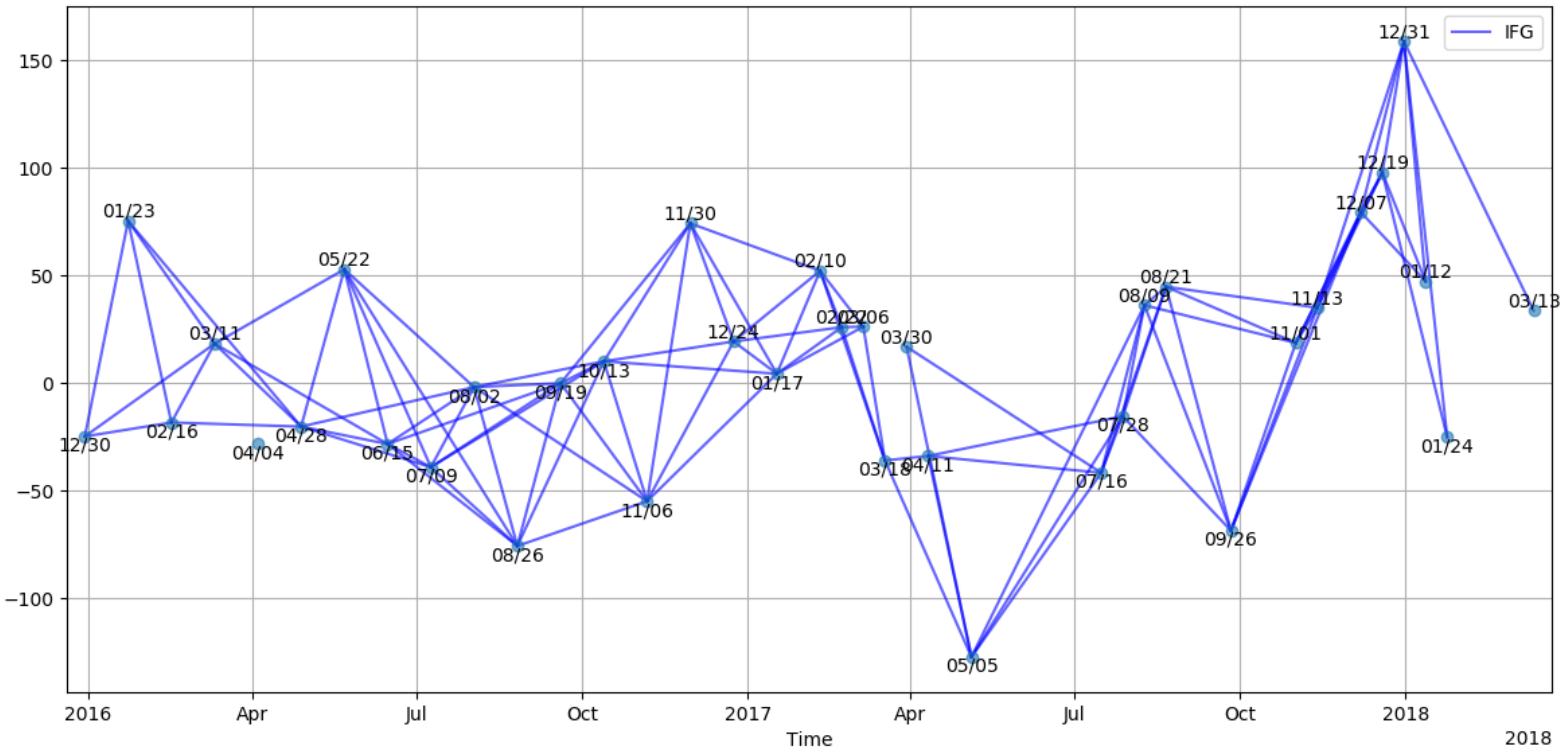

Figure S10. Perpendicular baseline (Bperp) against time for InSAR frame 100A_052 (Figs. 4 and S12). Lines indicate combination of acquired images to compute differential interferograms.

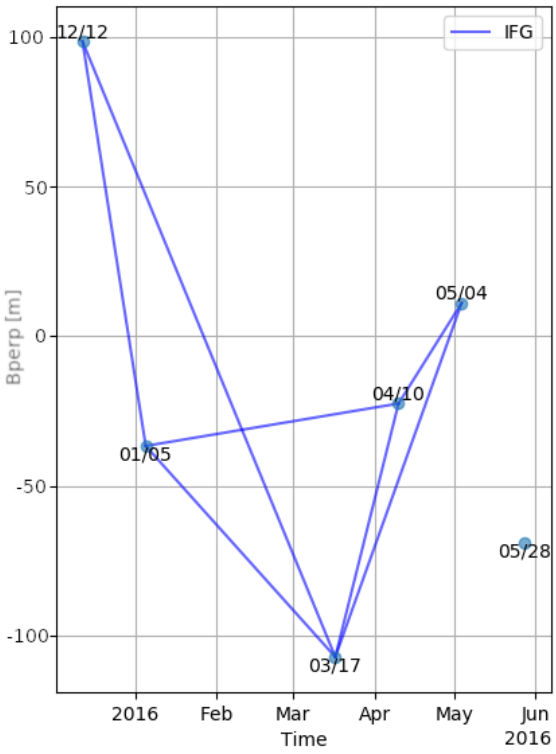

Figure S11. As Fig. S10, but for frame 005D_050.

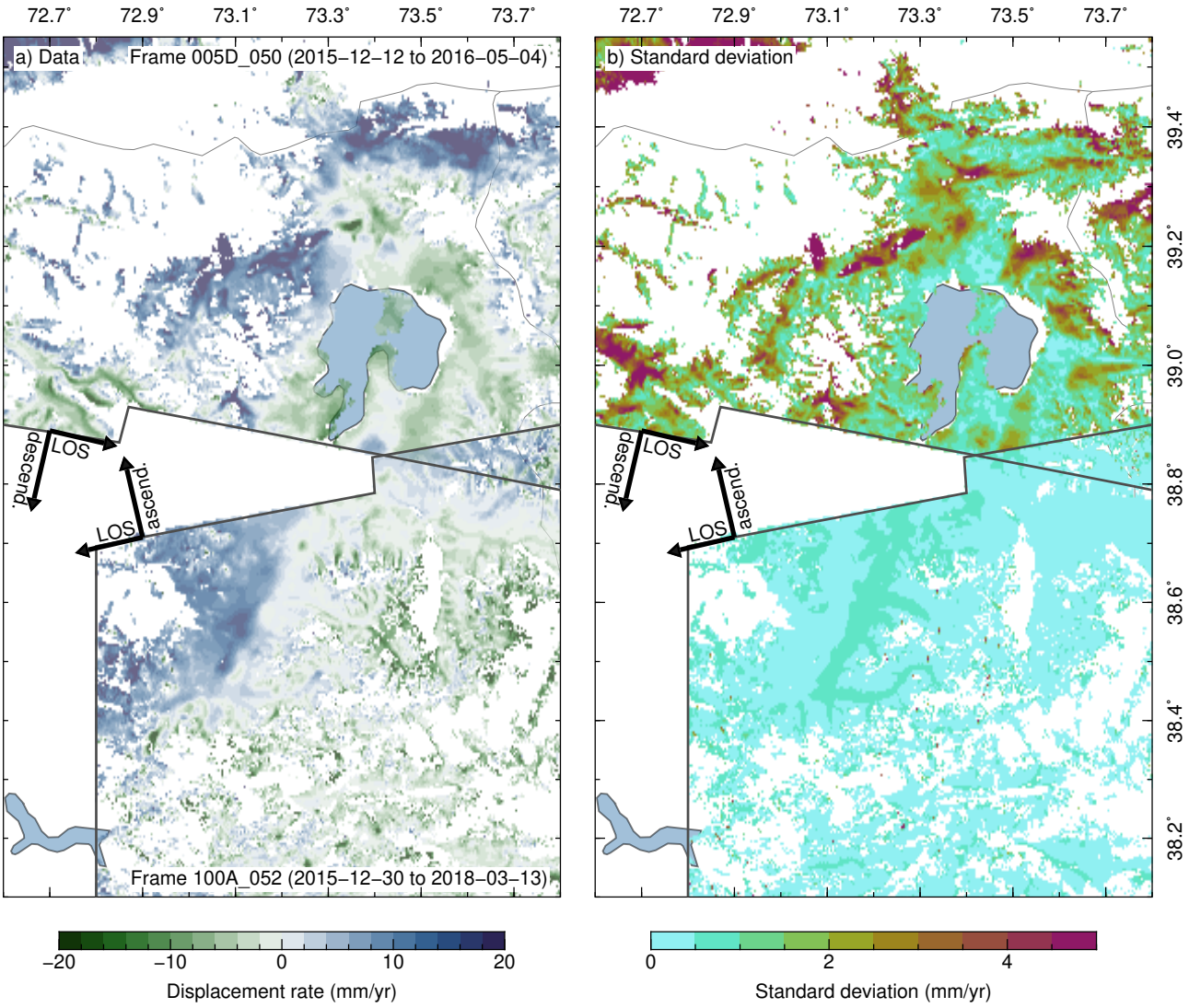

Figure S12. InSAR time series as in Fig. 5 of the main text. Left: rate map before conversion to displacement. Right: Nominal uncertainty of displacement rate.

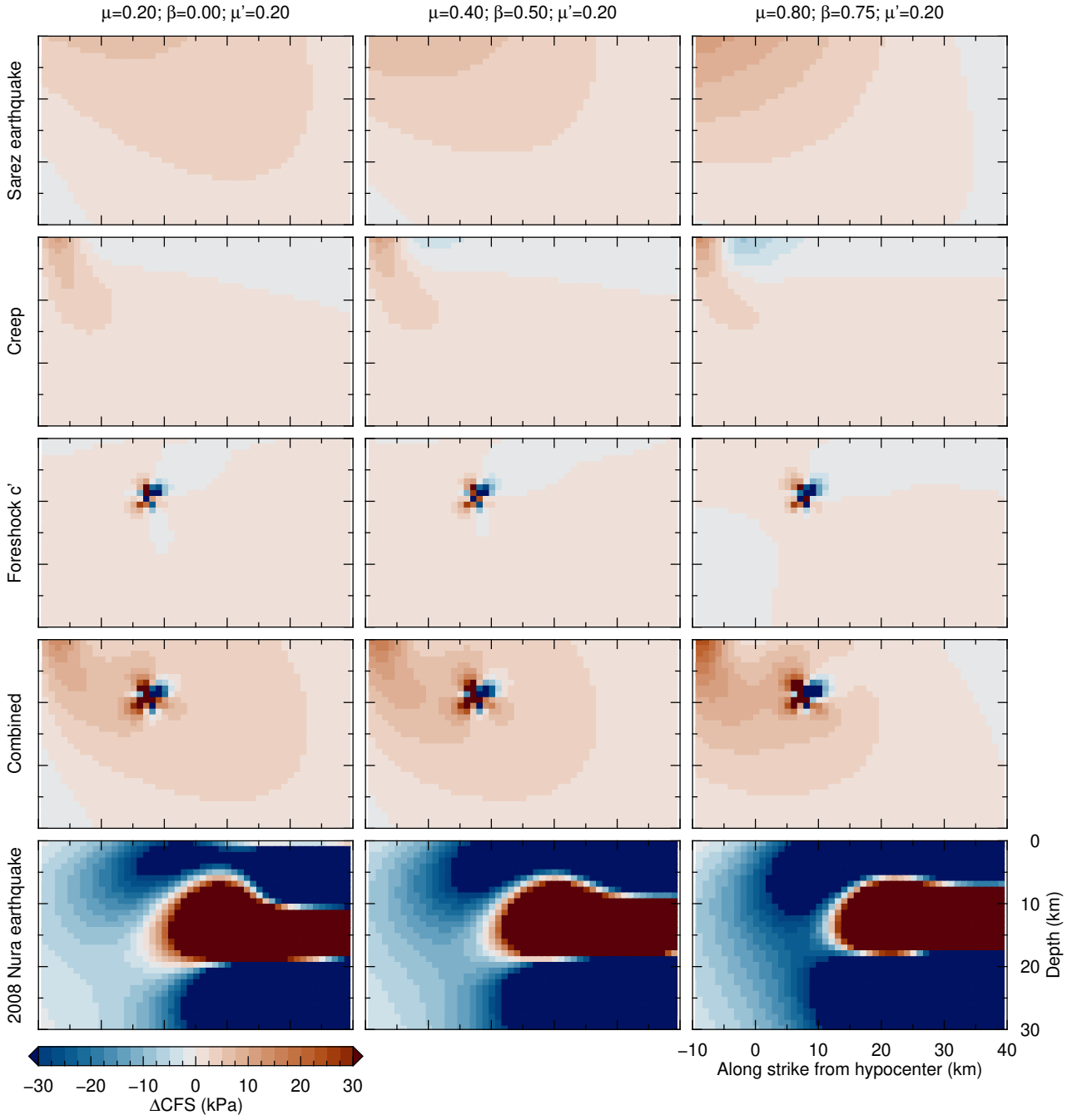

Figure S13. Contributions of distinct stress sources to the change in Coulomb failure stress (ΔCFS) on the fault plane of the Sary-Tash earthquake in dependence of friction (μ) and Skempton's parameter (β) under constant apparent friction (μ').

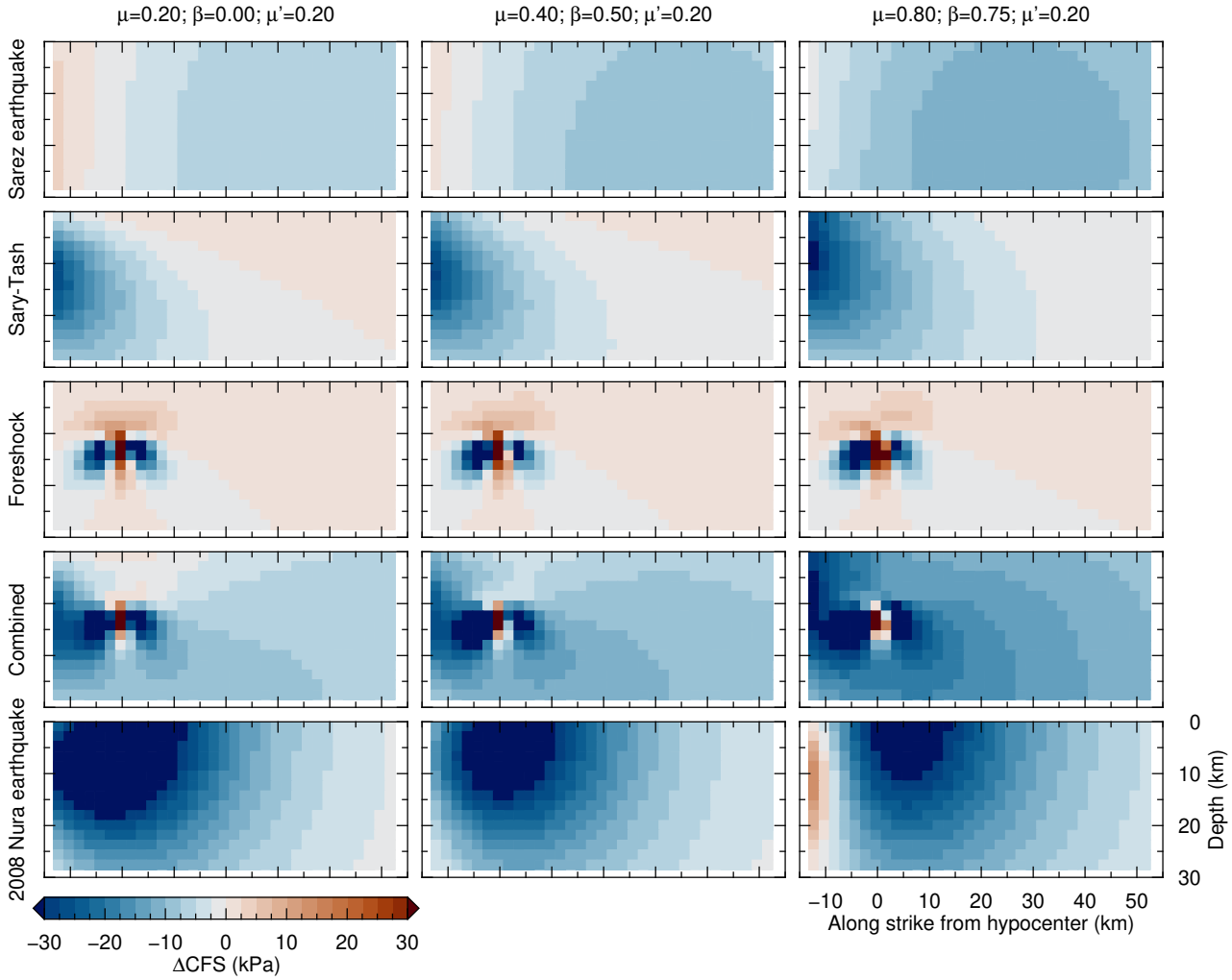

Figure S14. As Fig. S13, but for the Muji earthquake.

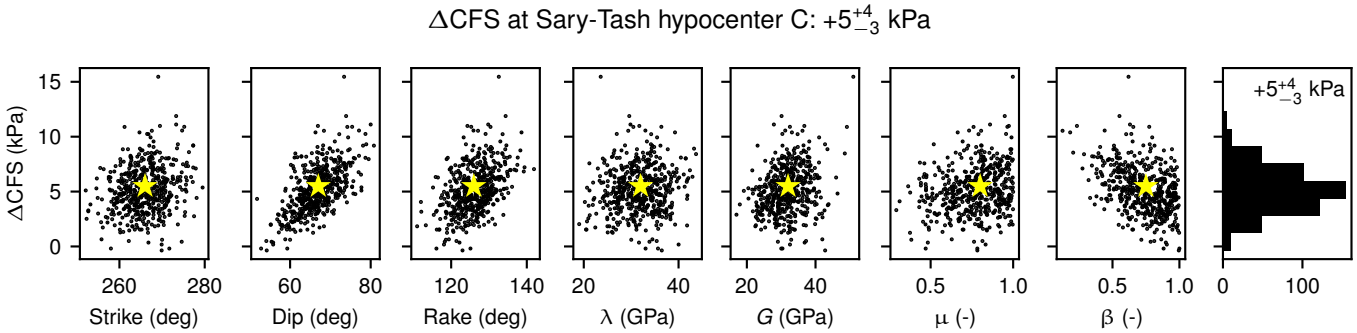

Figure S15. Sensitivity analysis of Coulomb failure stress changes at the Sary-Tash hypocenter *C** due to the Sarez earthquake, postseismic slip on the Sarez fault and foreshock *e'*. Contributions (from left to right) of normal distributed variations around the preferred values (stars)of receiver fault's strike, dip and rake (with a standard deviation of 5°), Lamé's parameters λ and G (standard deviation of 5 GPa), friction coefficient μ, and Skempton's parameter β (standard deviation 0.2, ensuring [0, 1] range). Resulting median, 5% and 95% quantiles under the assumption of input uncertainties.

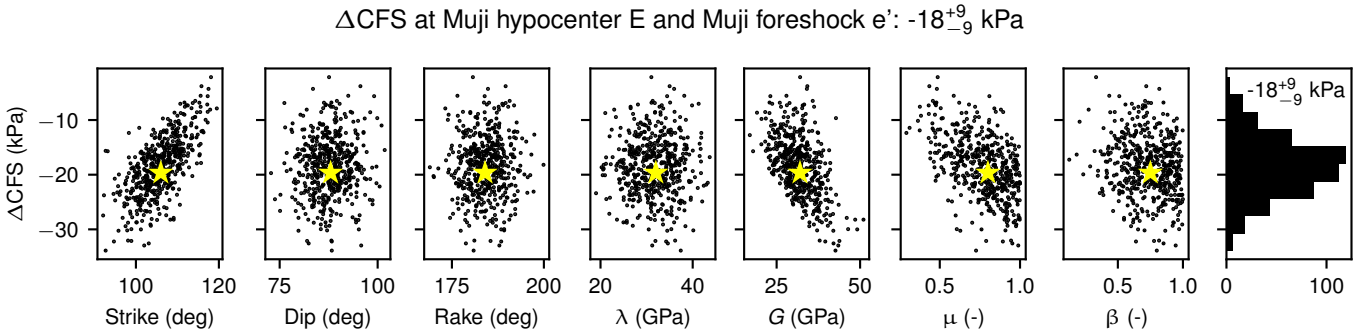

Figure S16. Sensitivity analysis of Coulomb failure stress changes as in Fig. S15, but due to the Sarez and Sary-Tash earthquakes at the Muji mainshock *E** or Muji foreshock *e'* hypocenter, both of which yield the same results within 100 Pa.